Acta Materialia 316 (2026) 122506

Contents lists available at ScienceDirect

Acta Materialia

journal homepage: www.elsevier.com/locate/actamat

Full length article

Correlation between enhanced oxygen evolution and β→γ phase transition in Mn-doped NiOOH

Da Chen [a], Filippo Bano [b], Daniele Perilli [a], Dario Mosconi [c], Lucio Litti [b], Stefano Agnoli [b], Annabella Selloni [d], Laura Calvillo [b,*], Cristiana Di Valentin [a,*]

[a] Department of Materials Science, Università degli Studi di Milano-Bicocca, Via Cozzi 55, 20125 Milano, Italy
[b] Dipartimento di Scienze Chimiche, Università di Padova and INSTM Research Unit, Via Marzolo 1, 35131 Padova, Italy
[c] Circular Materials s.r.l, Via Bragni, 93F, 35010, Padua, Italy
[d] Department of Chemistry, Princeton University, Princeton 08544 NJ, United States

ARTICLE INFO

Keywords:
OER
Mn-doped NiOOH
Phase transition
HSE06-D3
Overpotential
Cyclic voltammetry

ABSTRACT

NiOOH is a promising electrocatalyst for the oxygen evolution reaction (OER). Here we systematically investigate the effect of Mn doping on the structure, oxidation state, bond length, phase transition, and OER activity of NiOOH using dispersion-corrected hybrid density functional theory (HSE06+D3) combined with experimental material characterization and electrochemical measurements for samples that were prepared through a synthesis route mimicking Ni recovery from wastewater with circular-material benefits. Our results reveal that Mn doping promotes not only the formation of surface oxygen vacancies but also the phase transition from β- to γ-NiOOH, a critical step overlooked by previous studies. This Mn-doping is found to largely reduce the calculated overpotential, especially with respect to undoped β system, in very good agreement with experimental observations.

1. Introduction

With the rapid development of renewable energies, hydrogen has attracted widespread attention as a green secondary energy source. Water electrolysis is one of the ideal means to produce hydrogen due to its zero carbon emissions and high energy conversion efficiency. However, the oxygen evolution reaction (OER) occurring at the anode is generally limited by sluggish kinetics and high overpotential, which restrict the overall water splitting.

Precious metal catalysts such as IrO_2 and RuO_2 have excellent OER performance [1,2], but their high cost and scarcity limit their large-scale application. In contrast, $Ni(OH)_2$ has sparked intense research due to its abundance, low price and good OER activity under alkaline environments. Under an applied voltage, $Ni(OH)_2$ is oxidized to NiOOH, which is recognized to be the OER active phase [3–5]. However, the intrinsic OER activity of NiOOH still needs to be improved due to a high overpotential, about 0.68 V at 10 mA/cm^2 [6].

In addition to heterogeneous interface engineering with other layered materials or metals, such as MoS_2, Ni or Ag, etc. [7–11], anion intercalation has recently emerged as an effective strategy to enhance the OER activity of NiOOH. It was shown that anion insertion could promote the formation of γ-NiOOH with high-valence Ni^{4+} species, thereby significantly improving both the OER activity and stability [12–14]. Furthermore, doping strategies have also been widely used to control the electrocatalytic performance of NiOOH [4,6,15–20]. As a 3*d* transition metal, Mn can effectively regulate the redox behavior and charge transfer of NiOOH due to its rich variety of oxidation states (Mn^{2+}, Mn^{3+}, Mn^{4+}) and good affinity for oxygen, hence improving the OER activity of NiOOH [15,21–24]. However, due to the challenges of in-situ characterization of composition and structure during the OER, the active phase and structure-activity relationship of Mn-doped NiOOH in improving the OER performance have remained unclear [15,21–24].

Density functional theory (DFT) has been widely used to study the reaction mechanism of NiOOH catalysts [6,24–32]. DFT calculations can be used to elucidate the adsorption behavior of reactants on the catalyst surface, to identify the active site, and thus to infer the active phase, reaction path and mechanism, which are crucial for a more comprehensive understanding of experimental results. However, previous PBE+*U* calculations predicted that the overpotentials of the undoped and Mn-doped β-$Ni(OH)_2$ (0001) surface are 1.5 and 1.4 V, respectively, which are significantly larger than the experimentally measured values of 0.45 and 0.31 V at 100 mA/cm^2 [24]. Moreover, combined

* Corresponding authors.
E-mail addresses: laura.calvillolamana@unipd.it (L. Calvillo), cristiana.divalentin@unimib.it (C. Di Valentin).

https://doi.org/10.1016/j.actamat.2026.122506
Received 21 February 2026; Received in revised form 10 June 2026; Accepted 27 June 2026
Available online 28 June 2026

PBE+*U*/HSE06 calculations predicted that Mn doping increases the overpotential of NiOOH by 0.22 V, from 0.48 V for the undoped β-NiOOH ($\bar{1}2\bar{1}1$) surface to 0.70 V for the Mn-doped case [28], which is in contrast with the experimental observation that Mn doping significantly improves the OER performance of NiOOH [15,21,22,24].

Transition metal oxides are known to be strongly correlated systems, with the *d*-orbital electrons of the transition metal exhibiting localized behavior. Standard DFT methods, such as the widely used PBE functional, usually underestimate the band gap of transition metal oxides and overestimate the binding energy of adsorbates, thus failing to describe the electronic structure and adsorption behavior of the catalyst surface. To overcome these limitations, the in-situ coulomb correction term (DFT+*U*) [33] is commonly introduced to describe the transition metal *d* orbitals. However, previous calculations [26,27,29,31,34,35] indicate that the DFT+*U* method does not properly describe the electronic structure of β-NiOOH. For instance, it incorrectly predicts β-NiOOH to have metallic properties, which is inconsistent with the experimentally measured band gap of 1.7–1.8 eV [36]. In contrast, hybrid functionals, such as HSE06 [37], are capable of accurately predicting the band gap of β-NiOOH [27,29,31]. More importantly, previous calculations have proven that the use of hybrid functionals is also crucial for the description of the electronic structure dependent OER free-energy profiles [26,31].

On the other hand, existing theoretical studies generally ignore the effect that Mn-doping might have on the relative stability of different NiOOH phases and, consequently, on the OER activity [22–24,28]. Experimental observations show that undoped α-$Ni(OH)_2$ is unstable in alkaline solution transforming into the more stable β-$Ni(OH)_2$ through aging and becoming oxidized to β-NiOOH under applied potential [23,38,39]. In contrast, Mn doping tends to inhibit the formation of β-Ni$(OH)_2$/β-NiOOH and instead favors the formation of α-Ni$(OH)_2$/γ-NiOOH [15,22–24]. For the synthesized Mn-doped $Ni(OH)_2$ films, the substitution of Ni^{2+} with Mn^{3+} indeed requires additional anions and associated water to be inserted into the interlayer to maintain the electrical neutrality [15,21–24].

In this work, we use DFT calculations based on the HSE06 functional with Grimme's D3 dispersion corrections [40,41] (HSE06+D3) in combination with experimental material characterization and electrochemical measurements to systematically study the role of Mn doping on the phase transition, bonding properties, oxidation state, oxygen vacancy formation energy, surface active site and OER activity of NiOOH, and finally elucidate its structure-activity relationship. Our results indicate that Mn doping promotes the β to γ phase transition in NiOOH, regulates the bond lengths, and increases the Ni ions oxidation state, thereby optimizing the adsorption energy of the OER intermediates and significantly lowering the OER overpotential. Based on these results we can rationalize the observed boosting of the OER activity by NiOOH upon Mn doping in terms of the lower energy cost to create surface oxygen (O) vacancies and the induced β to γ phase transition, which are both key factors for improving the OER performance of NiOOH.

2. Experimental section

2.1. Computational details

The structural optimizations (fully optimized) and investigation of oxygen evolution reaction (OER) activity were carried out within the CRYSTAL17 package [42], using the Heyd–Scuseria–Ernzerhof (HSE06) hybrid functional [37], combined with Grimme's D3 (BJ) dispersion corrections [40,41]. The Kohn–Sham wavefunctions were expanded in Gaussian-type orbitals with the POB-TZVP-REV2 all-electron basis set. An electronic energy convergence threshold of 10^{-6} Hartree was employed, together with a 3 × 3 × 3 *k*-point mesh. For surface models, four-layer (0001)-(2 × 2) slabs containing 16 Ni atoms (4 atoms per layer) were constructed for NiOOH. The upper two layers were fully relaxed, while the bottom two layers were kept fixed. A vacuum spacing of 500 Å was applied along the surface normal to avoid inter-slab interactions under 2D periodic boundary conditions. Zero-point vibrational energy, entropy, and enthalpy contributions at 298.15 K were obtained from phonon calculations within the HSE06+D3 framework. Free energies of H_2O(l), gas phase N_2(g), H_2(g) and O_2(g) at standard temperature and pressure (298.15 K, 1 bar) were also computed by HSE06+D3 method, the same approach adopted in our previous work [31]. Structural visualization and analysis were carried out using VESTA [43].

2.2. Computational methodology for OER under electrocatalytic conditions

To explore the OER free energy diagram under electrocatalytic conditions, we firstly optimized the reaction intermediates to obtain the total electronic energies (*E*), which were subsequently corrected to Gibbs free energies (*G*) by including enthalpic and entropic contributions. The influence of the applied external potential was incorporated using the Computational Hydrogen Electrode (CHE) model developed by Nørskov et al. [44], which enabled the estimation of the overpotential (η). This model is warranted as our focus lies in comparative analysis of overpotential trends between pure and doped systems, rather than absolute overpotential values.

2.3. Synthesis and characterization of $Ni(OH)_2$ and Mn-doped $Ni(OH)_2$

Nickel hydroxide samples with different Mn doping (0 at.%, 3 at.%, 5 at.%, 8 at.%) were prepared by Circular Materials S.r.l. following a patented method [45], using manganese and nickel acetates (Mn$(CH_3COO)_2$, Ni$(CH_3COO)_2$, Sigma-Aldrich) as metal precursors and supercritical water as solvent. Briefly, the corresponding amount of Mn$(CH_3COO)_2$ was added to 0.5 L of a 0.3 M Ni$(CH_3COO)_2$ solution. Using the Circular Materials srl continuous flow pilot plant, the metal-containing solution was firstly pumped in the plant and mixed with a stream of 1 M NaOH to adjust the pH. Such obtained solution was then driven by pumps to the plant reactor, where the material precipitation occurs thanks to the mixing with a third stream of supercritical water (430 °C; 220 bar). The estimated residence time in the reactor is 1 – 2 s. Following to the reaction step, the final stream is cooled down and depressurized. The relative flows of the streams can be individually tuned to set the experiment conditions, which for these materials were 270 °C (reactor temperature) and pH 13 at the plant output. Subsequently, the solution was centrifuged to obtain the final material that was dried in an oven at 105 °C overnight. Finally, the solid grains were grinded into a fine powder in a mortar. Samples were labelled as *X*Mn-Ni$(OH)_2$, where *X* refers to the atomic Mn doping that is equal to 3, 5, 8. For simplicity, the undoped sample was just labelled as $Ni(OH)_2$.

Raman spectroscopy was performed to determine the phase of the pristine $Ni(OH)_2$ and electrochemically formed NiOOH-based materials. Raman spectra were obtained with an InVia micro-Raman system (Renishaw), under a 514 nm excitation at 1 mW on sample plate. The instrument is equipped with a Leica microscope, 10x or 50x magnification objectives are used in a backscattering configuration for excitation and collection. Exposition time is set to 30 s. All spectra are finally baseline subtracted and noise reduced. Grazing incidence X-ray diffraction (GIXRD) patterns of the $Ni(OH)_2$-based samples were acquired with a Bruker D8 Advance, operating with Cu K_α radiation (λ = 0.15406 nm) generated at 40 kV and 40 mA, before and after ageing treatments.

The morphology and microstructure of the samples were characterized by transmission electron microscopy (TEM) and high-angle annular dark-field (HAADF) scanning transmission electron microscopy (HAADF-STEM) using TEM JEOL F200 operated at 200 kV. Elemental analysis and mapping were performed using a JEOL 100 mm^2 silicon drift energy dispersive X-ray spectrometer (EDX). A lacey carbon

supported copper grid, 400 mesh size, was used for preparation of the sample.

X-ray photoemission spectroscopy (XPS) measurements were acquired in a custom-made UHV system working at a base pressure of 10^{-10} mbar, equipped with an Omicron EA125 electron analyser and an X-ray source with a dual Al−Mg anode. Core-level photoemission spectra (C 1 s, O 1 s, Mn 2p and Ni 2p) were collected at room temperature with a non-monochromatized Mg K_α X-ray source (1253.6 eV) using a 0.1 eV step, 0.5 s dwell time and pass energy 20.

2.4. Electrochemical characterization of $Ni(OH)_2$ and Mn-doped $Ni(OH)_2$

Electrochemical measurements were conducted in a three-electrode cell using a Hg/HgO electrode as a reference electrode and a graphite rod as a counter electrode. All the experiments were performed at room temperature. The working electrode was a glassy carbon (GC) electrode (3 mm diameter) modified with 5 μL of catalyst ink. The ink was prepared by mixing 3 mg of catalyst, 500 μL milli-Q water, 100 μL isopropyl alcohol and 10 μL of Nafion® (5 wt%, SigmaAldrich) and sonicating until a homogeneous dispersion was formed. Previously to the GC modification with the catalyst by drop casting, it was polished with 1 μm and 0.25 μm diamond pastes and sonicated in isopropyl alcohol. Cyclic (CVs) and linear sweep voltammetries (LSVs) were acquired at 5 mV s^{-1} in N_2-saturated 1 M KOH electrolyte, prepared from high purity reagents (Sigma-Aldrich). All the LSVs reported in this work are IR corrected. The ohmic drop resistance in the solution was determined by electrochemical impedance spectroscopy (12 Ω for the 1 M KOH solution). The ohmic drop compensation was performed during the data treatment. Currents reported in the text are normalized by the electroactive surface area (ECSA), determined from the Ni^{3+}/Ni^{2+} reduction peak according to the formula [46]: $\mathrm{ECSA} = \frac{peak\ \ area}{scan\ \ rate \cdot 2.75 \cdot 10^{-4}}$. Potential values are referenced to the reversible hydrogen electrode (RHE) by using the following equation: $E_{RHE} = E_{Hg/HgO} + 0.098 + 0.059\ pH$, where $E_{Hg/HgO}$ is the experimentally measured potential against the Hg/HgO reference electrode.

Tafel slopes were derived from steady-state polarization data obtained via chronoamperometry at fixed overpotentials in the onset potential region. The steady-state polarization curves were constructed by sampling the OER current density at 240 s, at which the current approached a stable value. A potential increment of 0.010 V was used within the catalytic turnover region. This approach ensures sufficiently stabilized current responses for reliable Tafel analysis, in line with established steady-state methodologies [47,48].

$Ni(OH)_2$ and 8Mn-$Ni(OH)_2$ samples were subjected to an aging treatment consisting of 10,000 potential cycles between 1.2 V and 1.7 V vs RHE at 50 mV/s.

3. Results and discussions

3.1. Surface models of stoichiometric and oxygen deficient NiOOH

We focus on surface models that expose the (0001) facet of NiOOH. In fact, previous DFT calculations have shown that this facet is the most abundant and thermodynamically stable surface, as indicated by the computed surface energies of 0.320 J/m^2 in vacuum and 0.192 J/m^2 in aqueous environment, which are significantly lower than the corresponding surface energies of 0.579 J/m^2 and 0.445 J/m^2, respectively, of the second most stable $(10\bar{1}0)$ facet [49,50]. In addition, previous experimental and computational studies found the O vacancy rather than the OH vacancy on the NiOOH surface to be the active site for the OER [31,51].

To start with, we investigated the oxygen vacancy formation energies to identify the most favorable active site on the NiOOH (0001) surface without/with Mn doping at different sites. For β-NiOOH, theoretical studies have proposed several candidate structures, namely U, L, S, and M phases [29,34,52]. In this work, U phase (β-NiOOH-U) was adopted since it resulted to be the most thermodynamically stable among these candidates [29,31]. In β-NiOOH, the top-layer Ni sites (denoted as site 1, 2, 3, and 4 in Fig. 1) can be categorized into two distinct types, notably sites 1 & 2 vs. sites 3 & 4, due to differences in their local coordination environments—specifically, the distortion of surface O–H bonds compared to the vertical O–H bonds forming hydrogen bonds with the second layer. For the β-NiOOH surface with an oxygen vacancy, denoted as β-NiOOH-V_O, Ni1, Ni2, and Ni4 are five-fold coordinated, whereas Ni3 remains six-fold coordinated. For γ-NiOOH, we used the model proposed by Friebel et al. [6], obtained by partial deprotonation of β-NiOOH to form a β-$NiOOH_{1-x}$ (x = 0.5) structure corresponding to an average Ni oxidation state of +3.5. Although the intercalated species are neglected due to their ambiguous experimental characterization, this model was shown to capture the experimentally relevant oxidation states and local coordination environments of Ni sites [6]. The validity of this model is further supported by our previous study which indicate that the inclusion of intercalated water has only a minor effect on the calculated overpotential [31]. For γ-NiOOH, there are three distinct types of Ni sites in the top layer, with only site 1 equivalent to site 3 based on their local configuration. As in β-NiOOH-V_O, Ni3 of γ-NiOOH-V_O maintains a six-coordinated bonding configuration, while the other sites are in a five-coordinated environment due to the formation of one oxygen vacancy.

Table 1 summarizes the oxygen vacancy formation energies ($\triangle G_f$) of NiOOH without/with Mn doping at different Ni sites. For undoped β-NiOOH, the computed $\triangle G_f$ is about 1.14 eV when the O atom is removed from the top layer. In the case of Mn-doped β-NiOOH, all the investigated doping configurations exhibit $\triangle G_f$ values larger than 1.14 eV, the lowest value being 1.22 eV for Mn substituting Ni3 (Mn3-doped). In contrast, all computed $\triangle G_f$ values for γ-NiOOH without/with Mn doping are smaller than that of β-NiOOH. Among them, Mn3-doped γ-NiOOH exhibits the lowest $\triangle G_f$ of 0.49 eV, which is smaller than the value of 0.66 eV for undoped γ-NiOOH and less than half the value for undoped β-NiOOH. This result is in agreement with O XPS (X-ray Photoelectron Spectroscopy) spectra reported in the literature, showing that Mn doping promotes the formation of oxygen vacancies [53,54]. Furthermore, our calculated oxygen vacancy formation energies support the experimental finding that Mn doping favors defectivity in NiOOH [15,22–24].

3.2. OER by pristine and Mn-doped NiOOH

3.2.1. Computational free energy profiles for OER

To clarify the role of Mn doping in enhancing the OER activity of NiOOH, we investigate the OER free energy profiles, according to the mechanism proposed by Qi Hu et al. [29], for both undoped and Mn3-doped β- and γ-NiOOH (see Fig. 2 and Table 2). We focus on the Mn3 doping site because it has the lowest oxygen vacancy formation energy in both the β- and γ- phases. We wish to stress that, in the case of this specific system (NiOOH), it is not possible to identify a “classical” AEM (Adsorbate Evolving Mechanism), nor a “classical” LOM (Lattice Oxygen Mechanism) due to the lack of undercoordinated surface metal atoms. The mechanism proposed by Qi Hu et al. [29] is not exactly AEM nor LOM but something in between, where, during the catalytic cycle, the O vacancies are continuously refilled by radical OH species to restart the reaction process.

As illustrated in Fig. 2a and b, Mn doping significantly increases the OER overpotential to 0.913 V for β-NiOOH compared to 0.675 V for the undoped case. This overpotential rise of 0.24 V is very close to the reported 0.22 V increase for the β-NiOOH $(\bar{1}2\bar{1}1)$ surface upon Mn doping obtained using combined PBE+*U*/HSE06 calculations [28]. However, this trend is clearly at odds with our experimental findings (see below) as well as previous results reported in the literature [15,21,22,24], which consistently demonstrate that Mn doping markedly enhances the

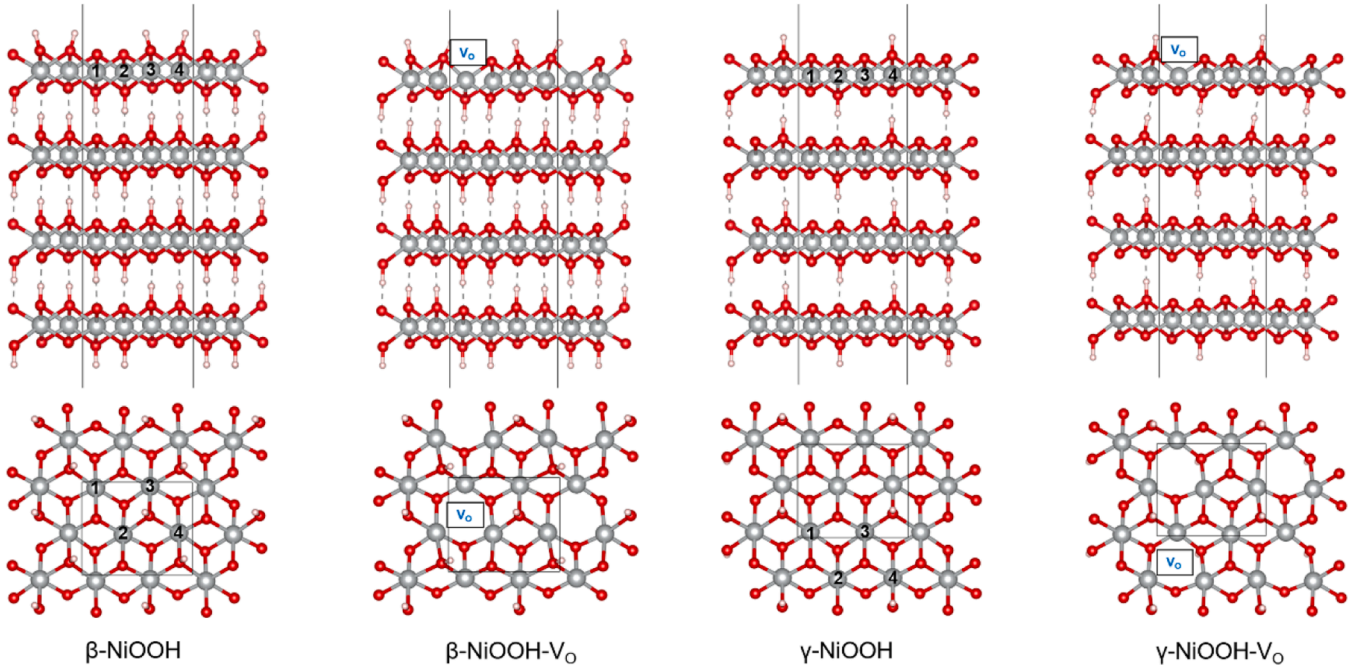

Fig. 1. Front and top views of (0001) facet of the four-layer slabs for β-NiOOH and γ-NiOOH, without/with an O vacancy (V_O) in the top layer. Ni sites are labeled as site 1, 2, 3 and 4.

Table 1
Oxygen vacancy formation energy (Gibbs free energy, $\triangle G_f$) of NiOOH without/with Mn doping at different Ni sites on the surface by HSE06+D3 method.

	$\triangle G_f$ (eV/top layer)	NiOOH → sub + ½ $O_{2(g)}$
β-NiOOH-U	undoped	1.14
	Mn1-doped	1.47
	Mn2-doped	1.61
	Mn3-doped	1.22
	Mn4-doped	1.87
γ-NiOOH	undoped	0.66
	Mn1-doped	1.07
	Mn2-doped	1.11
	Mn3-doped	0.49
	Mn4-doped	0.93

OER performance of NiOOH. For example, Yin et al. reported that a 26% Mn-doped α-$Ni(OH)_2$/γ-NiOOH film (where the initial α-$Ni(OH)_2$ phase converts to γ-NiOOH upon charging) exhibits an OER overpotential of only 0.309 V at 100 mA/cm^2, which is 0.136 V lower than that of undoped β-$Ni(OH)_2$/β-NiOOH system (0.445 V) [24]. Moreover, our calculations (Fig. 2a,b) indicate that Mn doping does not alter the potential determining O—O coupling step 3 ($*O + OH^- \rightarrow *OOH + e^-$) for the β-NiOOH (0001) surface.

To resolve the contradiction between the calculated increase of the OER overpotential of β-NiOOH upon Mn-doping and the experimental observation that Mn doping actually reduces the overpotential of NiOOH, and motivated by the fact that experiments indicate that Mn doping inhibits the formation of β-NiOOH and converts it to γ-NiOOH, we then turned to the investigation of the OER free energy profile for Mn3-doped γ-NiOOH. Encouragingly, Fig. 2d and Table 2 show that Mn doping lowers the OER overpotential of γ-NiOOH to 0.459 V, a significant decrease compared with the overpotential of pure β-NiOOH (0.675 V, Fig. 2a) and pure γ-NiOOH (0.514 V, Fig. 2c). This aligns well with our experimental electrochemical results shown below, and it confirms that Mn-doping improves the OER activity independently of the β-Ni$(OH)_2$/β-NiOOH or β-$Ni(OH)_2$/γ-NiOOH transitions. Clearly, Fig. 2 indicates that γ-NiOOH exhibits a significantly lower OER overpotential than β-NiOOH, which is consistent with previous experimental results demonstrating the superior OER activity of γ-NiOOH [3,4,12–14,55,56]. Moreover, Table 2 shows that steps 2 and 3 of Mn-doped γ-NiOOH have almost the same reaction free energies (1.686 vs. 1.689) and, thus, both are potential determining steps.

The above analysis of the OER free-energy profiles strongly supports the idea that Mn doping triggers a β- to γ-NiOOH phase transition and boosts the OER of NiOOH especially for the β phase. This hypothesis is further corroborated by our calculations of oxidation states, chemical bonds and formation energies in the next sections.

3.2.2. *Experimental measurements*

To confirm the role of Mn doping in enhancing the OER activity of NiOOH and compare it with our calculations, we prepared β-$Ni(OH)_2$ without and with different Mn-doping concentrations (3 at.%, 5 at.%, 8 at.%) and tested them as OER catalysts. For the synthesis, we employed the method used for the recovery of Ni from wastewater in collaboration with Circular Materials s.r.l. (see details in the ESI), as a preliminary study to validate the method for the preparation of Ni-based catalysts from circular nickel.

Regarding the electrochemical characterization, first, we determined the effect of Mn on the $Ni(OH)_2$ to NiOOH phase transformation. NiOOH is widely recognized as the active species in OER, and it is formed in situ under electrochemical conditions [57,58]. Cyclic voltammograms (CVs) reported in Fig. 3 show an oxidation peak between 1.4 V and 1.5 V in the forward scan that is attributed to the oxidation of Ni^{2+} ($Ni(OH)_2$) to Ni^{3+} (NiOOH), while the associated reduction peak is at approximately 1.3 V in the backward scan for all samples. A gradual shift of the Ni^{2+}/Ni^{3+} oxidation peak towards lower potentials is observed with increasing Mn content, indicating that Mn facilitates the oxidation of Ni species. This behavior is attributed to an electronic effect induced by Mn^{3+} on Ni^{2+}, as demonstrated in our previous work [59].

Next, we investigated the effect of Mn on the OER activity. Fig. 3b displays the linear sweep voltammograms (LSVs) recorded within the potential window relevant to the OER. A significant improvement in OER activity is observed upon Mn doping. All Mn-containing samples exhibit better performance compared to the undoped $Ni(OH)_2$, as evidenced by increased current densities and up to a 100 mV-shift of the onset potential towards lower values with increasing Mn content. This

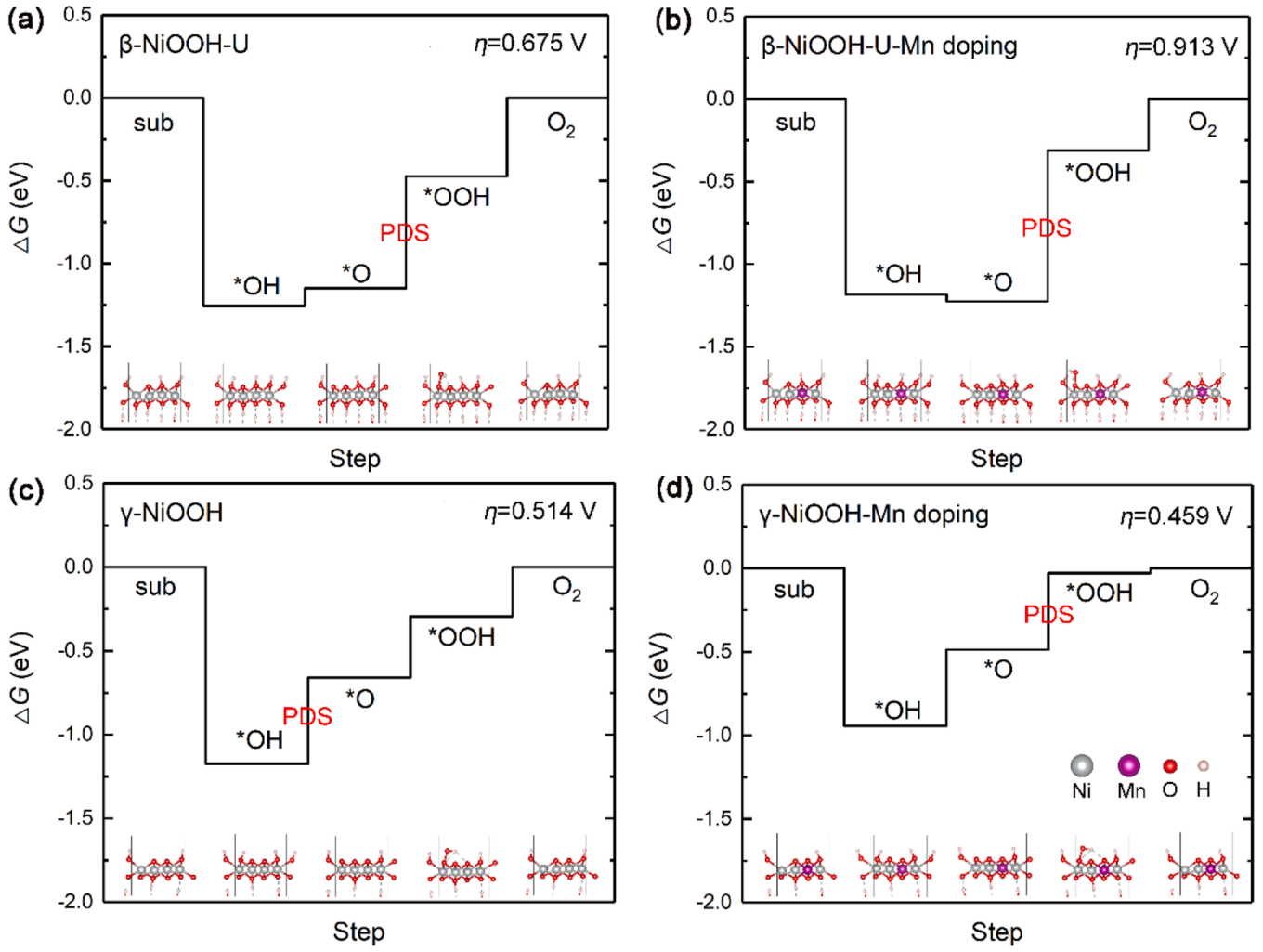

Fig. 2. OER free energy profiles from HSE06+D3 calculations on a four-layer slab model of (0001) surface without/with 25% Mn3 doping in the top layer: (a) and (b) β-NiOOH-U, (c) and (d) γ-NiOOH. The data of (a) and (c) are adapted from Ref. [31] for comparison. The reaction initiates at an O vacancy site for all cases. The label 'PDS' indicates the potential determining step.

Table 2
Calculated reaction free energies of the four OER steps at the O vacancy site on 25% Mn-doped β-NiOOH-U and γ-NiOOH (0001) surfaces using HSE06+D3.

	Step	Equation	Reaction free energy (eV)
Mn-doped β-NiOOH-U	1	$sub + OH^- \rightarrow *OH + e^-$	0.047
	2	$*OH + OH^- \rightarrow *O + H_2O + e^-$	1.189
	3	$*O + OH^- \rightarrow *OOH + e^-$	2.143 (η = 0.913)
	4	$*OOH + OH^- \rightarrow sub + O_2 + H_2O + e^-$	1.541
Mn-doped γ-NiOOH	1	$sub + OH^- \rightarrow *OH + e^-$	0.286
	2	$*OH + OH^- \rightarrow *O + H_2O + e^-$	1.686
	3	$*O + OH^- \rightarrow *OOH + e^-$	1.689 (η = 0.459)
	4	$*OOH + OH^- \rightarrow sub + O_2 + H_2O + e^-$	1.259

enhancement in catalytic activity is attributed to the reduced energy required for the formation of Ni^{3+} species (see Fig. 3a), which are known to be the active sites for OER.

Finally, we evaluated the reaction kinetics and investigated the effect of Mn incorporation on the OER pathway by means of steady-state Tafel analysis. As shown in Fig. 3c, the undoped sample exhibits a Tafel slope of approximately 48 mV dec^{-1}, lying between the characteristic values of 40 and 60 mV dec^{-1} commonly associated with different possible rate-determining steps, including *OH oxidation and *OOH formation. According to Zhao et al., a Tafel slope of approximately 50 mV dec^{-1} can be associated with the formation of *OOH as the rate-determining step [60].

In contrast, the Mn-doped samples display a slight decrease in Tafel slope with increasing Mn content, approaching 40 mV dec^{-1} (Fig. 3c). This trend suggests a shift toward kinetics dominated by *OOH formation, corresponding to the O–O coupling step. Importantly, the theoretical results presented in Fig. 2 identify the O–O coupling step ($*O + OH^- \rightarrow *OOH + e^-$) as the potential-determining step in Mn-doped NiOOH.

Therefore, while the Tafel analysis alone does not provide definitive mechanistic identification, the experimental trends are consistent with the theoretical predictions, providing supportive evidence for the proposed reaction pathway.

We further measured Raman spectra on both the $Ni(OH)_2$ and 8Mn–$Ni(OH)_2$ samples, before and after polarization at 1.6 V, to investigate the phase transformation induced under electrochemical conditions in the presence and absence of Mn. As shown in Figure S1a,b, both undoped and Mn-doped $Ni(OH)_2$ samples show low intensity peaks at around 304 cm^{-1}, 450 cm^{-1} and a high intensity one at 3581 cm^{-1}, characteristic of β-$Ni(OH)_2$ [61]. In addition, they show a low intensity band at around 526 cm^{-1}, which is usually associated to defective or disordered $Ni(OH)_2$ [61–63]. 8Mn-$Ni(OH)_2$ exhibits, in addition, a wide

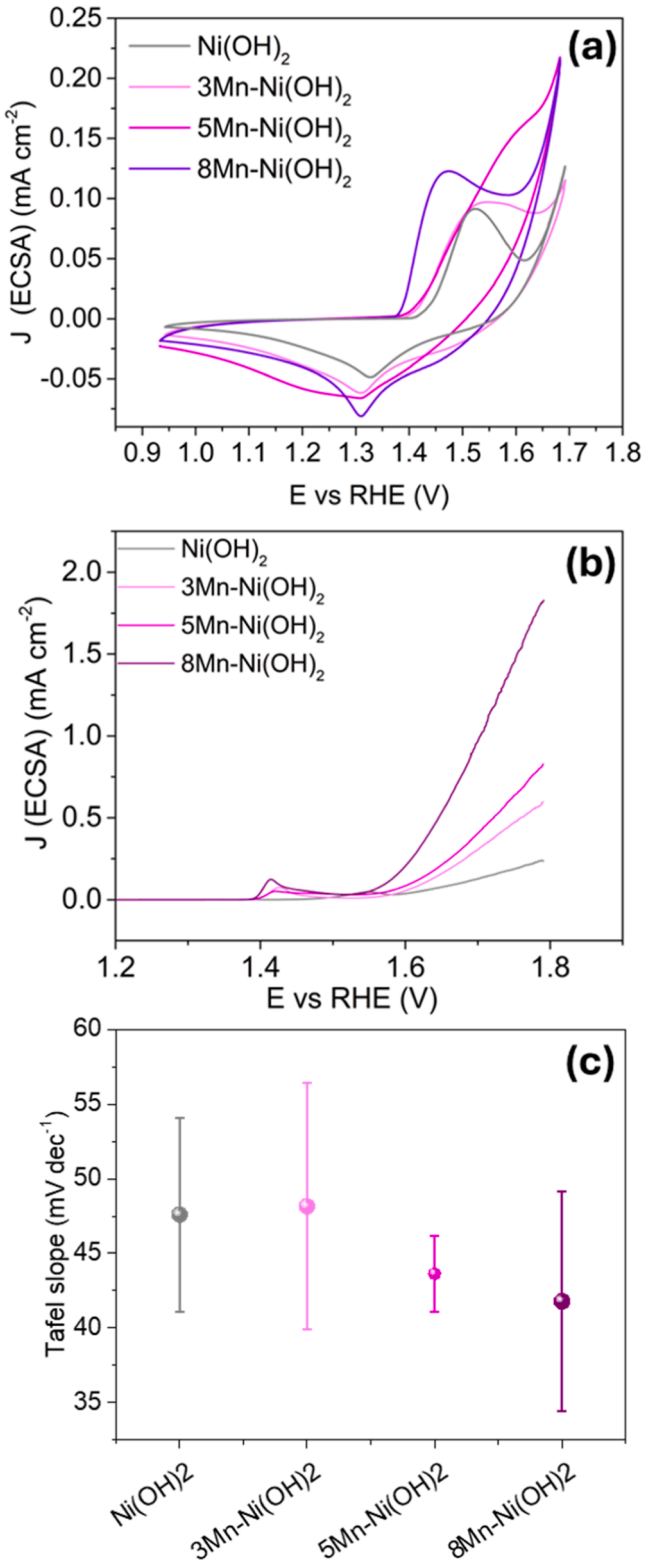

Fig. 3. (a) CVs and (b) LSVs in N_2-saturated 1 M KOH; and (c) Tafel analysis for the β-$Ni(OH)_2$ without and with Mn-doping. Current in (a) and (b) are normalized by ECSA (electrochemical surface area).

peak in the 600–625 cm^{-1} region, which is ascribed to Mn–O symmetric stretching vibrations [64,65]. Moreover, the peak at 3581 cm^{-1} for this sample is broader than that of the undoped sample, which is due to the defectivity/disorder introduced by the presence of Mn.

After the electrochemical conversion of $Ni(OH)_2$ into NiOOH, two peaks at 476 and 557 cm^{-1} are clearly observed for both polarized samples, which correspond to the formation of NiOOH, while the features associated with $Ni(OH)_2$ disappear (Figure S1c). These two vibrations are known to have high Raman cross section due to resonance effects, consistent with the higher signal-to-noise ratio for these peaks compared to the ones for the $Ni(OH)_2$ phase. The band at 557 cm^{-1} arises from the Ni–O stretching vibration (A_{1g} mode) characteristic of NiOOH, whereas the band at 476 cm^{-1} is assigned to the E_g bending vibration of Ni–O in NiOOH [65,66]. Both the β- and γ-NiOOH phases exhibit this pair of peaks, while the intensity ratio between the two is often used to quantify the relative amounts of β- and γ-NiOOH. Specifically, the intensity ratio of the 476 cm^{-1} band to the 557 cm^{-1} band is thought to be much lower for β-NiOOH (close to 1) than for γ-NiOOH (greater than 1) [63,65,67,68]. In our study, the ratio of the two bands is the same and greater than 1, both in the presence and the absence of Mn. Therefore, it seems that γ-NiOOH corresponds to the observed phase, even for the undoped case. However, in the literature it has also been reported that the ratio of the two bands is not very different for the β and γ phases in some cases, 1.42 for β versus 1.55 for γ [55], making it very difficult to identify the phase, or the presence of both of them and their percentage, only by considering their intensity ratio. Moreover, it was reported that NiOOH can be both in the β or γ phase depending on the aging or overcharging or freezing [3,4,34,56,69], see Table S3, indicating that the phase of undoped NiOOH depends on the experimental conditions. For this reason, in the computational analysis in the section below we will consider both phases for the undoped case.

To complement the Raman results on our samples, we also analyzed the $Ni(OH)_2$ and 8Mn-$Ni(OH)_2$ ones after an aging treatment by XRD (details in the Experimental section). Figure S2 shows the grazing-incidence X-ray diffraction (GIXRD) patterns of thin films of $Ni(OH)_2$ and 8Mn–$Ni(OH)_2$ drop-cast onto a glassy carbon substrate, both before and after the ageing treatment. The pristine $Ni(OH)_2$ sample exhibits the characteristic (001) and (100) reflections of β-$Ni(OH)_2$, in agreement with the Raman spectroscopy results. The 8Mn–$Ni(OH)_2$ sample displays the same reflections, confirming the formation of the β-phase in the presence of Mn. However, the diffraction peaks of the Mn-doped sample are noticeably broader, indicating a higher degree of structural disorder associated with the incorporation of Mn ions into the $Ni(OH)_2$ lattice. In both samples, the (002) and (004) reflections originating from the glassy carbon substrate are also observed. After the aging treatment, the diffraction patterns undergo a significant transformation, showing only the (003) and (006) reflections characteristic of γ-NiOOH [70,71]. This finding is fully consistent with the ex-situ Raman spectra recorded after OER polarization of the same samples, as well as with our theoretical calculations, which predict a β-to-γ phase transition under OER conditions.

To assess the possible dissolution or loss of Mn during catalysis and to evaluate any morphological changes, X-ray photoemission spectroscopy (XPS) and transmission electron microscopy (TEM) analyses, complemented by selected area electron diffraction (SAED) and energy dispersive X-ray spectroscopy (EDS) measurements, were carried out on the aged 8Mn–$Ni(OH)_2$ sample.

Figure S3 presents representative TEM images of the material before and after the ageing treatment. The pristine 8Mn–$Ni(OH)_2$ sample exhibits the characteristic layered morphology of $Ni(OH)_2$, consisting of small nanorods approximately 5 nm in diameter and 15–20 nm in length (Figures S3a,b). The formation of the β-phase is further confirmed by the SAED pattern shown in Figure S4a. The measured interplanar spacings of the Mn-doped sample closely match those of a reference $Ni(OH)_2$ material. A slight reduction in the interplanar distances is observed upon Mn incorporation, consistent with the lattice contraction reported in the literature and in our previous work [24,59,72]. After the cycling treatment, no significant morphological changes are observed (Figures S3c, d), indicating excellent structural stability. However, the interplanar spacings change substantially and become fully consistent with those of γ-NiOOH, as evidenced by the SAED pattern shown in Figure S4b. This

finding is in excellent agreement with the GIXRD and Raman spectroscopy results, which also indicate the formation of the γ-NiOOH phase under OER conditions.

The elemental mapping results for the pristine and aged samples (Figs. S3e–l) reveal a homogeneous distribution of Ni, Mn, and O throughout the material. The Ni:Mn atomic ratio determined by EDS is 6.5 for the pristine sample and 7.0 for the aged sample, values that are very close to the nominal composition and to those previously determined by ICP–MS and XPS [59]. These results provide strong evidence that Mn remains incorporated in the catalyst structure and that no detectable Mn dissolution occurs during the ageing treatment.

XPS analysis was performed on the 8Mn–Ni(OH)₂ sample to complement the structural information obtained from XRD and TEM. Figure S5 presents the Ni 2p and Mn 2p spectra of the sample before and after the ageing treatment. As reported in our previous work [59], all pristine samples exhibit essentially identical Ni 2p spectra, characteristic of Ni(OH)₂, and an excellent fit was obtained using only the peaks corresponding to this component, with no need to introduce additional components associated with other nickel-containing phases. Figure S5a compares the Ni 2p region of the 8Mn–Ni(OH)₂ sample before and after the ageing treatment. Following cycling, the Ni $2p_{3/2}$ peak shifts slightly toward lower binding energies, while the intensity of the satellite features decreases relative to the pristine material. These spectral changes are characteristic of the transformation from Ni(OH)₂ to γ-NiOOH and are in excellent agreement with literature reports for γ-NiOOH [73]. The XPS results, therefore, provide additional evidence supporting the phase transition identified by GIXRD, Raman spectroscopy, and TEM analyses.

The Mn 2p spectra are presented in Figure S5b. It should be noted that both spectra exhibit a relatively low signal-to-noise ratio due to the low Mn content in the samples, which limits the accuracy of the spectral analysis. Nevertheless, no significant differences are observed in the Mn 2p region before and after the ageing treatment. The spectral features are consistent with the presence of Mn^{4+} species at the particle surface, which can be attributed to the partial oxidation of Mn^{3+} upon exposure to air, in agreement with previous reports [22].

In summary, the post-mortem characterization provides strong and complementary evidence for the β-to-γ phase transition occurring under OER conditions. Furthermore, the combined XRD, TEM, EDS, and XPS analyses demonstrate the excellent morphological and chemical stability of the Mn-doped material throughout the ageing treatment, with no detectable Mn loss and preservation of the catalyst morphology.

3.3. Analysis of spin configuration and oxidation state of Ni and Mn ions

The oxidation states of Ni and Mn were determined based on the atomic spin densities calculated using the HSE06+D3 functional as implemented in CRYSTAL17 code [42]. The same methodology has been widely employed in prior theoretical studies [26,27,29,34]. Our calculations indicate that all the Ni cations in the pristine β-NiOOH-U (0001) surface adopt a Ni^{3+} low-spin (LS) d^7 ($t_{2g}^6 e_g^1$) configuration (see Fig. 4), in line with previous calculations [26,27,29,34]. For β-NiOOH doped with 25% Mn in the top layer, our analysis reveals that Mn^{4+} replaces one LS Ni^{3+} in the top layer, resulting in a charge transfer that reduces an adjacent Ni^{3+} to LS Ni^{2+}, with the average oxidation state of Ni decreasing to +2.7. This reduction in the oxidation state of surface Ni cations suppresses the catalytic activity, explaining why Mn-doped β-NiOOH exhibits a higher OER overpotential than the pure case. A similar trend was found in previous calculations [28], where Mo or Cr doping was predicted to drastically increase the OER overpotential of β-NiOOH to about 2.3 and 1.2 V, respectively, which are much higher than that of pristine β-NiOOH (0.5 V). This is because Mo or Cr is readily oxidized to its highest oxidation state (+6) [28], which, in turn, reduces three adjacent active Ni^{3+} cations to inactive Ni^{2+} for Cr or Mo-doped β-NiOOH, thereby resulting in a significant increase in the calculated overpotential compared to that of pure β-NiOOH. These calculations, however, do not explain why experiments observed that Mo or Cr doping enhances the OER activity of NiOOH [74,75].

One possible reason for the discrepancy between the above computational and experimental results is that previous calculations [24,28] generally ignore the role of Mn (or Mo, Cr) doping on the β- to γ-NiOOH phase transition. Experiments show that in Mn(or Mo, Cr)-doped Ni $(OH)_2$ films, the substitution of Ni^{2+} cations by Mn^{3+} (or Mo^{6+}, Cr^{3+}) requires the incorporation of additional anions and associated water into the interlayer to maintain the electrical neutrality [15,21–24,74,75]. Consequently, such doping suppresses the formation of β-NiOOH film and instead promotes the stabilization of γ-NiOOH, as seen in Figure S1c [15,21–24,74,75]. We propose that this is likely the reason why experiments [15,21–24,74,75] observe that doping with Mn (or Mo, Cr) improve the OER activity of NiOOH, whereas this is not the case in computational studies [28].

To confirm this possibility, we investigated the oxidation states of Mn-doped γ-NiOOH. Our calculations indicate that Mn^{4+} prefers to replace one LS Ni^{4+} in the top layer (which contains two Ni^{3+} and two Ni^{4+} cations in the case of pure γ-NiOOH), so that the average oxidation state of Ni is +3.3 for Mn-doped γ-NiOOH. Based on this analysis, Mn doping increases the average oxidation state of Ni from +3 to +3.3 by promoting the phase transition from β- to γ-NiOOH, a result that is also supported by the investigation of bond lengths (see below).

3.4. Analysis of structural parameters

Table 3 lists the average M–O bond lengths (M = Ni, Mn) in the top layer of pure and 25% Mn-doped β-/γ-NiOOH (0001), with the detailed values provided in Table S2. For undoped β-NiOOH-U, the average Ni–O bond length (AvNi–O) is 1.941 Å, whereas Mn doping increases it to 1.972 Å. This elongation of the Ni–O bonds for β-NiOOH-U arises from the reduction of the Ni oxidation state from +3 to +2.7 upon Mn substitution, as confirmed by the oxidation-state analysis in the previous section. Although the average Mn–O bond length (AvMn–O = 1.887 Å, Mn^{4+}) is significantly shorter than the AvNi–O (1.941 Å, Ni^{3+}) of

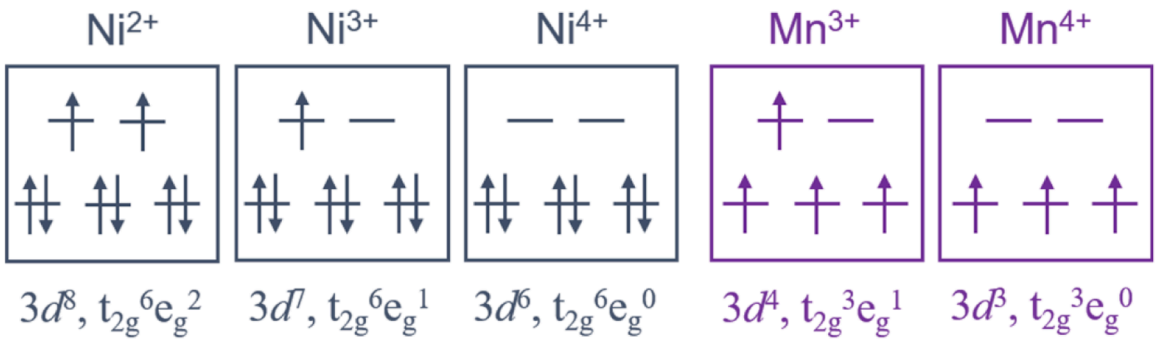

Fig. 4. The 3*d* orbital distributions and corresponding oxidation states of Ni and Mn cations.

Table 3
M–O (M = Ni, Mn) bond lengths of the top layer for pure and 25% Mn-doped β-/γ-NiOOH (0001) surface by HSE+D3 method. AvMn–O and AvNi–O denote the average Mn–O and Ni–O bond length, respectively. AvALL represents the average M–O bond length over all Mn–O or Ni–O bonds. More details are reported in Table S2.

Bond length (Å)	Mn–O	Ni–O	AvALL
β-NiOOH-U	N/A	AvNi–O = 1.941	1.941
Mn-doped β-NiOOH-U	AvMn–O = 1.887	AvNi–O = 1.972	1.951
γ-NiOOH	N/A	AvNi–O = 1.918	1.918
Mn-doped γ-NiOOH	AvMn–O = 1.894	AvNi–O = 1.936	1.925

β-NiOOH-U, the average M–O bond length over all Mn–O or Ni–O bonds (AvALL) of Mn-doped β-NiOOH-U (1.951 Å) remains lager than that for the undoped case (1.941 Å). In contrast, Mn doping in γ-NiOOH reduces the AvNi–O to 1.936 Å compared with that of β-NiOOH-U (1.941 Å). This is in agreement with our previous experimental results [59], which strongly supports that Mn doping induces the β to γ phase transition in NiOOH. Specifically, the decrease in Ni–O bond length from β-NiOOH-U to Mn-doped γ-NiOOH corresponds to an increase in the average Ni oxidation state from +3.0 to +3.3, see above oxidation-state analysis. Together with the shorter Mn–O bonds, this leads to a smaller AvALL (1.925 Å) than that of β-NiOOH-U (1.941 Å). In addition to the above bond length analysis, our phase transition energy analysis (see below) also supports that Mn doping tends to induce the β→γ phase transition in NiOOH.

3.5. Energetics of phase transition

To form γ-NiOOH, two H atoms from surface OH groups of β-NiOOH were removed (top layer) with the lower three layers kept unmodified, ensuring consistency with our model in which the doping effect was investigated for the top layer of a four-layer slab. Calculations were performed under two conditions: vacuum and oxygen-rich environments.

In the first case (vacuum condition), the β→γ phase transition is modeled as the direct deprotonation and oxidation of the β-NiOOH top layer, forming a top layer of γ-NiOOH and releasing one gaseous H_2 molecule. The free energy (1 atm, 300 K) of the phase transition is thus defined as: $\Delta G_{pt} = G_{\gamma\text{-NiOOH}} + G_{H2,(g)} - G_{\beta\text{-NiOOH}}$, where $G_{\gamma\text{-NiOOH}}$, $G_{H2,(g)}$ and $G_{\beta\text{-NiOOH}}$ are the free energies of γ-NiOOH, gaseous H_2, and β-NiOOH, respectively. As shown in Table S2, Mn doping reduces ΔG_{pt} from +4.52 eV for undoped NiOOH to +4.05 eV for Mn-doped system.

In the second case, the phase transition is considered to occur in a more realistic oxygenated environment according to the following equation:

$$\beta\text{-NiOOH} + \tfrac{1}{2}\, O_{2,(g)} \rightarrow \gamma\text{-NiOOH} + H_2O_{,(l)}.$$

Compared to Table S2, the free energy (1 atm, 300 K) of the phase transition illustrated in Fig. 5 indicates that the oxygen environment markedly lowers ΔG_{pt} (defined as $\Delta G_{pt} = G_{\gamma\text{-NiOOH}} + G_{H2O,(l)} - G_{\beta\text{-NiOOH}} - \tfrac{1}{2}\, G_{O2,(g)}$, where $G_{H2O,(l)}$ is the free energy of liquid H_2O) from +4.52 (vacuum case) to +2.06 eV (oxygen-rich case) for the undoped NiOOH. Doping further decreases ΔG_{pt} to +1.59 eV for the Mn-doped NiOOH, with a decrease of 23%, relative to the undoped case in the oxygen environment, see Fig. 5. These results again demonstrate that Mn doping substantially facilitates the β→γ phase transition in NiOOH.

We further studied the effect of O_2 partial pressure/concentration on the phase transition free energy (ΔG_{pt}) from β-NiOOH to γ-NiOOH (top layer) [76–78]. We set the temperature to 300 K to approximate the general experimental conditions. At the specified temperature, the effect of O_2 pressure on the reaction free energy can be described as a function of the O chemical potential, as illustrated in Fig. 5. Clearly, ΔG_{pt} of both undoped and 25% Mn-doped NiOOH decreases with increasing O_2 pressure, suggesting that γ-NiOOH are more easily formed under O-rich

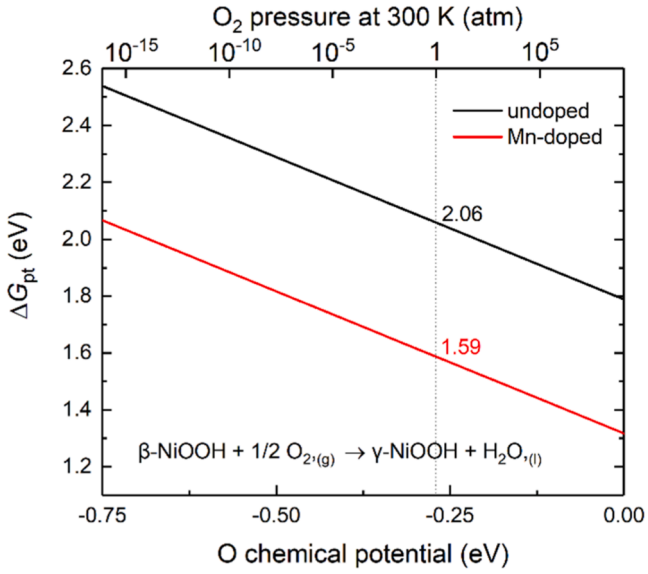

Fig. 5. Phase transition free energy (ΔG_{pt}) from β-NiOOH to γ-NiOOH (top layer) as a function of the O chemical potential and O_2 partial pressure for the undoped and 25% Mn-doped NiOOH calculated by the HSE06+D3 method.

conditions. The formation of γ-NiOOH involves a positive formation energy since an external voltage is required to trigger this transition, whereas a much lower voltage is needed for the Mn-doped system. Moreover, this phase transition process is strongly influenced by pH, with higher pH values (alkaline conditions) promoting this transition.

Notably, ΔG_{pt} values at 1 atm in Fig. 5 indicate that Mn doping significantly decreases the energy barrier for the β- to γ-NiOOH phase transition to 1.59 eV, compared with 2.06 eV for pure NiOOH. This value is even lower than that of the Fe-doped system (1.86 eV) reported in our previous work [31]. Combined with the results in Table 2, which show that Mn-doped γ-NiOOH exhibits an OER overpotential similar to that of the Fe-doped system [31], Mn emerges as a promising dopant for enhancing the OER activity of NiOOH. This conclusion is consistent with a previous analysis that used the adsorption energies of *O and *OH [79] as descriptors of the OER activity.

We also note that although Table 1 indicates that Mn doping lowers the O vacancy formation energy to 0.49 eV, compared with 1.14 eV for the pure system, Fe doping exhibits an even lower formation energy (0.22 eV). This suggests that Fe more effectively promotes oxygen vacancy generation, thereby facilitating the onset of the OER. Regarding oxidation states, both Mn and Fe with an oxidation state of +4 facilitate the oxidation of Ni by promoting the β- to γ-NiOOH phase transition, which is supported by the analyses of oxygen vacancy energy, bond length, and phase transition energy. The phase transition is further corroborated by experimental findings showing that substitution of Mn^{3+} or Fe^{3+} for Ni^{2+} in $Ni(OH)_2$ induces additional anion and H_2O insertion into the interlayer, leading to the β-$Ni(OH)_2$/β-NiOOH to α-$Ni(OH)_2$/γ-NiOOH transition [4,6,22,24]. Our calculations reveal this phase transition is the crucial step in enhancing the OER activity of NiOOH. Therefore, transition metals with high oxidation states (≥3) are recommended as dopants for improving the OER activity of $Ni(OH)_2$/NiOOH films.

4. Conclusions

In conclusion, our HSE06+D3 calculations combined with experimental data from electrochemical measurements provide coherent atomic-level insights into the active phase and mechanism by which Mn doping enhances the OER performance of NiOOH. The formation energy of the oxygen vacancy ($\triangle G_{pt}$) is drastically reduced in Mn-doped

γ-NiOOH (0.49 eV) especially compared to that of undoped β-NiOOH (1.14 eV), in line with previous experimental observations (based on XPS spectra) that Mn doping promotes the formation of oxygen vacancies [53,54]. Phase transition energies indeed prove that Mn doping significantly stabilize the γ-NiOOH phase over the β phase thermodynamically, both in vacuum and, more realistically, in oxygen-rich environments. Oxidation state and chemical bond analysis also support this transition. These modifications collectively optimize the adsorption free energies of OER intermediates on the Mn-doped γ-NiOOH (0001) surface. The calculated overpotential of Mn-doped γ-NiOOH (0.459 V) is lower than that of the undoped material, especially for β-NiOOH (0.675 V). Combined with our previous studies of Fe-doped NiOOH [31], transition metals with high oxidation states (≥3) are recommended as dopants to enhance the OER activity of $Ni(OH)_2$/NiOOH films. This work not only elucidates the specific mechanism for Mn-doped NiOOH but also establishes the doping-induced phase transition as a vital design principle for developing high-performance, non-precious metal-based OER catalysts.

Data availability statement

The data that support the conclusions in this study are present in the paper and the Supplementary Information and are available from the corresponding author upon reasonable request.

Supporting Information

Calculation details, experimental details, bond length, phase transition free energy.

CRediT authorship contribution statement

Da Chen: Writing – original draft, Visualization, Investigation, Formal analysis, Data curation. **Filippo Bano:** Writing – review & editing, Visualization, Investigation, Formal analysis, Data curation. **Daniele Perilli:** Writing – review & editing, Validation, Formal analysis. **Dario Mosconi:** Writing – review & editing, Investigation. **Lucio Litti:** Writing – review & editing, Investigation, Formal analysis, Data curation. **Stefano Agnoli:** Writing – review & editing, Formal analysis. **Annabella Selloni:** Writing – review & editing, Formal analysis. **Laura Calvillo:** Writing – review & editing, Supervision, Resources, Project administration, Funding acquisition, Formal analysis, Conceptualization. **Cristiana Di Valentin:** Writing – review & editing, Supervision, Resources, Project administration, Funding acquisition, Formal analysis, Conceptualization.

Declaration of competing interest

The authors declare that they have no known competing financial interests or personal relationships that could have appeared to influence the work reported in this paper.

Acknowledgements

The authors thank Lorenzo Ferraro for technical support. The authors thank the high-performance computing resources of University of Milano-Bicocca. This work has been supported by the project "Hydrogen, electricity, and clean water from recycled nickel and urea" funded by the MIUR Progetti di Ricerca di Rilevante Interesse Nazionale (PRIN 2022 PNRR-M4C2I1.1) - Grant P2022FALAP. C.D.V. would like to acknowledge the National Recovery and Resilience Plan (PNRR), Mission 2 "Green Revolution and Ecological Transition", Component 2 "Renewable Energy, Hydrogen, Network and Sustainable Mobility", Investment 3.5 "Hydrogen Research and Development", European Union – Next Generation EU – Ministry of Ecological Transition, project AMBITION.

Supplementary materials

Supplementary material associated with this article can be found, in the online version, at doi:10.1016/j.actamat.2026.122506.

References

[1] J. Rossmeisl, Z.-W. Qu, H. Zhu, G.-J. Kroes, J.K. Nørskov, Electrolysis of water on oxide surfaces, J. Electroanal. Chem. 607 (1–2) (2007) 83–89.
[2] Y. Lee, J. Suntivich, K.J. May, E.E. Perry, Y. Shao-Horn, Synthesis and activities of rutile IrO_2 and RuO_2 nanoparticles for oxygen evolution in acid and alkaline solutions, J. Phys. Chem. Lett. 3 (3) (2012) 399–404.
[3] D.K. Bediako, B. Lassalle-Kaiser, Y. Surendranath, J. Yano, V.K. Yachandra, D. G. Nocera, Structure–activity correlations in a nickel–borate oxygen evolution catalyst, J. Am. Chem. Soc. 134 (15) (2012) 6801–6809.
[4] L. Trotochaud, S.L. Young, J.K. Ranney, S.W. Boettcher, Nickel–iron oxyhydroxide oxygen-evolution electrocatalysts: the role of intentional and incidental iron incorporation, J. Am. Chem. Soc. 136 (18) (2014) 6744–6753.
[5] F. Dionigi, Z. Zeng, I. Sinev, T. Merzdorf, S. Deshpande, M.B. Lopez, S. Kunze, I. Zegkinoglou, H. Sarodnik, D. Fan, In-situ structure and catalytic mechanism of NiFe and CoFe layered double hydroxides during oxygen evolution, Nat. Commun. 11 (1) (2020) 2522.
[6] D. Friebel, M.W. Louie, M. Bajdich, K.E. Sanwald, Y. Cai, A.M. Wise, M.-J. Cheng, D. Sokaras, T.-C. Weng, R. Alonso-Mori, Identification of highly active Fe sites in (Ni, Fe) OOH for electrocatalytic water splitting, J. Am. Chem. Soc. 137 (3) (2015) 1305–1313.
[7] Y. Li, J. Han, W. Bao, J. Zhang, T. Ai, M. Yang, C. Yang, P. Zhang, Self-derivation and reconstruction of silver nanoparticle reinforced cobalt-nickel bimetallic hydroxides through interface engineering for overall water splitting, J. Energy Chem. 90 (2024) 590–599.
[8] L. Du, L.B. Chen, X. Liu, C.C. Yang, Q. Jiang, Heterogeneous interface and vacancy engineering contribute to metastable catalysts for overall water splitting, Acta. Mater. 289 (2025) 120934.
[9] S. Yang, J. Han, W. Bao, T. Ai, X. Wei, P. Jiang, Z. Deng, J. Zhang, NiVFe-LDH nanosheets reinforced MoS_2 heterogeneous interface design for glycol-assisted water electrolysis, Fuel 388 (2025) 134482.
[10] X. Zhao, H. Zhao, X. Du, X. Zhang, The NiS_2/FeS/MoS_2@NF as an efficient bifunctional electrode for urea assisted water splitting, J. Taiwan Inst. Chem. Eng. 183 (2026) 106649.
[11] Y. Wu, X. Du, X. Zhang, Fe-doped $CoMoO_4$/Ni_3S_2 grown on Ni foam as a multifunctional electrode for electrocatalytic seawater and urea splitting, J. Alloy. Compd. 1030 (2025) 180927.
[12] Y. Li, Q. Li, S. Peng, Formamide-assisted synthesis of phosphate-intercalated Ni (OH)2/NiOOH electrode for boosting oxygen evolution reaction, J. Colloid Interface Sci. 689 (2025) 137209.
[13] Y. Li, J. Liu, S. Li, S. Peng, Codecoration of phosphate and iron for improving oxygen evolution reaction of layered $Ni(OH)_2$/NiOOH, ACS Catal. 14 (7) (2024) 4807–4819.
[14] Y. Li, R. Tong, W. Zhang, S. Peng, Pre-intercalation of phosphate into Ni(OH)2/NiOOH for efficient and stable electrocatalytic oxygen evolution reaction, J. Catal. 410 (2022) 22–30.
[15] Y. Wang, D. Yan, S. El Hankari, Y. Zou, S. Wang, Recent progress on layered double hydroxides and their derivatives for electrocatalytic water splitting, Adv. Sci. 5 (8) (2018) 1800064.
[16] Y. Chen, K. Rui, J. Zhu, S.X. Dou, W. Sun, Recent progress on nickel-based oxide/(oxy) hydroxide electrocatalysts for the oxygen evolution reaction, Chem. Eur. J. 25 (3) (2019) 703–713.
[17] X. Sun, W. Shen, H. Liu, P. Xi, M. Jaroniec, Y. Zheng, S.-Z. Qiao, Corrosion-resistant NiFe anode towards kilowatt-scale alkaline seawater electrolysis, Nat. Commun. 15 (1) (2024) 10351.
[18] J. Kim, J. Yoo, K. Lee, Unveiling the role of electrocatalysts activation for iron-doped Ni oxyhydroxide in enhancing the catalytic performance of oxygen evolution reaction, Energy Environ. Mater. 8 (2) (2025) e12827.
[19] A. Seijas-Da Silva, A. Hartert, V. Oestreicher, J. Romero, C. Jaramillo-Hernández, L.J. Muris, G. Thorez, B.J. Vieira, G. Ducourthial, A. Fiocco, Scalable synthesis of NiFe-layered double hydroxide for efficient anion exchange membrane electrolysis, Nat. Commun. 16 (1) (2025) 6138.
[20] G. Shi, J. Li, T. Lu, C. Yang, Q. Xu, H. Gu, H. Tong, S. Zhao, C. Zhu, Y. Shen, Lattice O–O ligands in Fe-incorporated hydroxides enhance water oxidation electrocatalysis, Nat. Chem. 17 (2025) 1607–1614.
[21] A. Sumboja, J. Chen, Y. Zong, P.S. Lee, Z. Liu, NiMn layered double hydroxides as efficient electrocatalysts for the oxygen evolution reaction and their application in rechargeable Zn–air batteries, Nanoscale 9 (2) (2017) 774–780.
[22] Z. Zhang, H. Huo, L. Wang, S. Lou, L. Xiang, B. Xie, Q. Wang, C. Du, J. Wang, G. Yin, Stacking fault disorder induced by Mn doping in $Ni(OH)_2$ for supercapacitor electrodes, Chem. Eng. J. 412 (2021) 128617.
[23] Z. Zhang, H. Huo, Z. Yu, L. Xiang, B. Xie, C. Du, J. Wang, G. Yin, Unraveling the reaction mechanism of low dose Mn dopant in $Ni(OH)_2$ supercapacitor electrode, J. Energy Chem. 61 (2021) 497–506.
[24] T.-T. Yin, H.-M. Xu, X.-L. Zhang, X. Su, L. Shi, C. Gu, S.-K. Han, Mn-incorporation-induced phase transition in bottom-up synthesized colloidal sub-1-nm $Ni(OH)_2$ nanosheets for enhanced oxygen evolution catalysis, Nano Lett. 23 (8) (2023) 3259–3266.

[25] Y.-F. Li, A. Selloni, Mechanism and activity of water oxidation on selected surfaces of pure and Fe-doped NiO x, ACS Catal. 4 (4) (2014) 1148–1153.
[26] Z.K. Goldsmith, A.K. Harshan, J.B. Gerken, M. Vörös, G. Galli, S.S. Stahl, S. Hammes-Schiffer, Characterization of NiFe oxyhydroxide electrocatalysts by integrated electronic structure calculations and spectroelectrochemistry, Proc. Natl. Acad. Sci. USA 114 (12) (2017) 3050–3055.
[27] J.M.P. Martirez, E.A. Carter, Unraveling oxygen evolution on iron-doped β-nickel oxyhydroxide: the key role of highly active molecular-like sites, J. Am. Chem. Soc. 141 (1) (2019) 693–705.
[28] J.M.P. Martirez, E.A. Carter, Noninnocent influence of host β-NiOOH redox activity on transition-metal dopants' efficacy as active sites in electrocatalytic water oxidation, ACS Catal. 10 (4) (2020) 2720–2734.
[29] Q. Hu, Y. Xue, J. Kang, I. Scivetti, G. Teobaldi, A. Selloni, L. Guo, L.-M. Liu, Structure and oxygen evolution activity of β-NiOOH: where are the protons? ACS Catal. 12 (1) (2022) 295–304.
[30] P. Ding, Q. Hu, Z. Chai, H.-B. Zhou, G.-H. Lu, G. Teobaldi, A. Selloni, L.-M. Liu, Distribution of high valence Fe sites in nickel–iron hydroxide catalysts for water oxidation, J. Mater. Chem. A 12 (5) (2024) 2830–2838.
[31] D. Chen, D. Perilli, R. Dronskowski, A. Selloni, C. Di Valentin, Enhanced oxygen evolution on NiOOH through Fe-promoted transformation of β to γ phase, Acta Mater. 299 (2025) 121434.
[32] G. Mattioli, L. Guidoni, Multiple reaction pathways for oxygen evolution as a key factor for the catalytic activity of nickel–Iron (Oxy) hydroxides, J. Am. Chem. Soc. 147 (8) (2025) 6450–6463.
[33] M. Cococcioni, S. De Gironcoli, Linear response approach to the calculation of the effective interaction parameters in the LDA+U method, Phys. Rev. B-Condens. Matter. Mater. Phys. 71 (3) (2005) 035105.
[34] A.J. Tkalych, K. Yu, E.A. Carter, Structural and electronic features of β-Ni$(OH)_2$ and β-NiOOH from first principles, J. Phys. Chem. C 119 (43) (2015) 24315–24322.
[35] J. Zaffran, M.C. Toroker, Benchmarking density functional theory based methods to model NiOOH material properties: hubbard and van der Waals corrections vs hybrid functionals, J. Chem. Theory Comput. 12 (8) (2016) 3807–3812.
[36] M.K. Carpenter, D.A. Corrigan, Photoelectrochemistry of nickel hydroxide thin films, J. Electrochem. Soc. 136 (4) (1989) 1022–1026.
[37] A.V. Krukau, O.A. Vydrov, A.F. Izmaylov, G.E. Scuseria, Influence of the exchange screening parameter on the performance of screened hybrid functionals, J. Chem. Phys. 125 (22) (2006).
[38] A. Šurca, B. Orel, B. Pihlar, P. Bukovec, Optical, spectroelectrochemical and structural properties of sol-gel derived Ni-oxide electrochromic film, J. Electroanal. Chem. 408 (1–2) (1996) 83–100.
[39] M.S. Kim, K.B. Kim, A study on the phase transformation of electrochemically precipitated nickel hydroxides using an electrochemical quartz crystal microbalance, J. Electrochem. Soc. 145 (2) (1998) 507–511.
[40] S. Grimme, J. Antony, S. Ehrlich, H. Krieg, A consistent and accurate ab initio parametrization of density functional dispersion correction (DFT-D) for the 94 elements H-Pu, J. Chem. Phys. 132 (15) (2010).
[41] S. Grimme, S. Ehrlich, L. Goerigk, Effect of the damping function in dispersion corrected density functional theory, J. Comput. Chem. 32 (7) (2011) 1456–1465.
[42] R. Dovesi, A. Erba, R. Orlando, C.M. Zicovich-Wilson, B. Civalleri, L. Maschio, M. Rérat, S. Casassa, J. Baima, S. Salustro, Quantum-mechanical condensed matter simulations with CRYSTAL, Rev. Comput. Mol. Sci. 8 (4) (2018) e1360.
[43] K. Momma, F. Izumi, VESTA 3 for three-dimensional visualization of crystal, volumetric and morphology data, J. Appl. Crystallogr. 44 (6) (2011) 1272–1276.
[44] J.K. Nørskov, J. Rossmeisl, A. Logadottir, L. Lindqvist, J.R. Kitchin, T. Bligaard, H. Jonsson, Origin of the overpotential for oxygen reduction at a fuel-cell cathode, J. Phys. Chem. B 108 (46) (2004) 17886–17892.
[45] M. Bersani, Method for treating wastewater for the recovery of metals contained therein, and apparatus for such a METHOD, Wo2021089403a1, 2021.
[46] J. Li, S. Wang, J. Chang, L. Feng, A review of Ni based powder catalyst for urea oxidation in assisting water splitting reaction, Adv. Powder Mater. 1 (3) (2022) 100030.
[47] J.O.M. Bockris, T. Otagawa, Mechanism of oxygen evolution on perovskites, J. Phys. Chem. 87 (15) (1983) 2960–2971.
[48] S. Anantharaj, S. Noda, M. Driess, P.W. Menezes, The pitfalls of using potentiodynamic polarization curves for tafel analysis in electrocatalytic water splitting, ACS Energy Lett. 6 (4) (2021) 1607–1611.
[49] J.M.P. Martirez, E.A. Carter, Effects of the aqueous environment on the stability and chemistry of β-NiOOH surfaces, Chem. Mater. 30 (15) (2018) 5205–5219.
[50] Y.-F. Li, J.-L. Li, Z.-P. Liu, Structure and catalysis of NiOOH: recent advances on atomic simulation, J. Phys. Chem. C 125 (49) (2021) 27033–27045.
[51] W. Chen, L. Xu, X. Zhu, Y.C. Huang, W. Zhou, D. Wang, Y. Zhou, S. Du, Q. Li, C. Xie, Unveiling the electrooxidation of urea: intramolecular coupling of the N−N bond, Angew. Chem. Int. Ed. 60 (13) (2021) 7297–7307.
[52] Y.-F. Li, A. Selloni, Mosaic texture and double c-axis periodicity of β-NiOOH: insights from first-principles and genetic algorithm calculations, J. Phys. Chem. Lett. 5 (22) (2014) 3981–3985.
[53] N.-N. Ge, C.-H. Gong, X.-C. Yuan, H.-Z. Zeng, X.-H. Wei, Effect of Mn doping On Electroforming and Threshold Voltages of Bipolar Resistive Switching in Al/Mn: NiO/ITO, 8, RSC Adv, 2018, pp. 29499–29504.
[54] Y. Liu, L. Bai, T. Li, J. Huo, X. Wang, L. Zhang, X. Hao, S. Guo, Mn-doping tuned electron configuration and oxygen vacancies in NiO nanoparticles for stable electrocatalytic oxygen evolution reaction, Appl. Surf. Sci. 577 (2022) 151952.
[55] S. Klaus, Y. Cai, M.W. Louie, L. Trotochaud, A.T. Bell, Effects of Fe electrolyte impurities on $Ni(OH)_2$/NiOOH structure and oxygen evolution activity, J. Phys. Chem. C 119 (13) (2015) 7243–7254.
[56] X. Cui, Y. Ding, F. Zhang, X. Cao, Y. Guo, L. Sun, B. Zhang, Reserved charges in a long-lived NiOOH phase drive catalytic water oxidation, Nat. Chem. (2025) 1–8.
[57] Š. Trafela, J. Zavašnik, S. Šturm, K.Ž. Rožman, Formation of a $Ni(OH)_2$/NiOOH active redox couple on nickel nanowires for formaldehyde detection in alkaline media, Electrochim. Acta. 309 (2019) 346–353.
[58] V.M. Zemtsova, A.G. Oshchepkov, E.R. Savinova, Unveiling the role of iron in the nickel-catalyzed urea oxidation reaction, ACS Catal. 13 (20) (2023) 13466–13473.
[59] F. Bano, D. Chen, D. Perilli, S. Zambonin, D. Mosconi, M. Roverso, V. Celorrio, C. Di Valentin, L. Calvillo, Enhanced urea oxidation reaction by Mn-doped nickel hydroxide from wastewater, Energy Environ. Mater. (2026) e70465.
[60] L. Zhao, K. Meng, Y. Guo, Q. Wu, Q. Zhu, T. Zhou, Y. Fu, M. Wen, FeCoP sub-nanometric-sheets for electrocatalzing overall water splitting, Nano Res. Energy 3 (4) (2024) e9120129.
[61] D.S. Hall, D.J. Lockwood, C. Bock, B.R. MacDougall, Nickel hydroxides and related materials: a review of their structures, synthesis and properties, Proc. R. Soc. A 471 (2174) (2015) 20140792.
[62] D.S. Hall, D.J. Lockwood, S. Poirier, C. Bock, B.R. MacDougall, Raman and infrared spectroscopy of α and β phases of thin nickel hydroxide films electrochemically formed on nickel, J. Phys. Chem. A 116 (25) (2012) 6771–6784.
[63] M.W. Louie, A.T. Bell, An investigation of thin-film Ni–Fe oxide catalysts for the electrochemical evolution of oxygen, J. Am. Chem. Soc. 135 (33) (2013) 12329–12337.
[64] J. Yang, B. Guo, H. He, Y. Li, C. Song, G. Liu, $LiNi_{0.5}Mn_{0.5}O_2$ hierarchical nanorods as high-capacity cathode materials for Li-ion batteries, J. Alloys Compd. 698 (2017) 714–718.
[65] X. Yang, H. Zhang, W. Xu, B. Yu, Y. Liu, Z. Wu, A doping element improving the properties of catalysis: in situ raman spectroscopy insights into Mn-doped NiMn layered double hydroxide for the urea oxidation reaction, Catal. Sci. Technol. 12 (14) (2022) 4471–4485.
[66] X. Du, W. Han, X. Zhang, Application of in situ Raman and other technique in electrocatalytic water splitting, Int. J. Hydrog. Energy 200 (2026) 152918.
[67] X. Bo, R.K. Hocking, S. Zhou, Y. Li, X. Chen, J. Zhuang, Y. Du, C. Zhao, Capturing the active sites of multimetallic (oxy) hydroxides for the oxygen evolution reaction, Energy Environ. Sci. 13 (11) (2020) 4225–4237.
[68] B.S. Yeo, A.T. Bell, In situ Raman study of nickel oxide and gold-supported nickel oxide catalysts for the electrochemical evolution of oxygen, J. Phys. Chem. C 116 (15) (2012) 8394–8400.
[69] M. Morishita, S. Ochiai, T. Kakeya, T. Ozaki, Y. Kawabe, M. Watada, S. Tanase, T. Sakai, Phase transformation in the charge-discharge process and the structural analysis by synchrotron XAFS and XRD for nickel hydroxide electrode, Electrochem 76 (11) (2008) 802–807.
[70] R.P. Putra, I.B. Rachman, H. Horino, I.I. Rzeznicka, γ-NiOOH electrocatalyst derived from a nickel dithiooxamide chelate polymer for oxygen evolution reaction in alkaline solutions, Catal. Today 397-399 (2022) 308–315.
[71] P.C. Laan, F.J. de Zwart, E.M. Wilson, A. Troglia, O.C. Lugier, N.J. Geels, R. Bliem, J.N. Reek, B. de Bruin, G. Rothenberg, Understanding the oxidative properties of nickel oxyhydroxide in alcohol oxidation reactions, ACS Catal. 13 (13) (2023) 8467–8476.
[72] C. Mahala, M. Devi Sharma, M. Basu, Fe-doped nickel hydroxide/nickel oxyhydroxide function as an efficient catalyst for the oxygen evolution reaction, Chem. Electro. Chem. 6 (13) (2019) 3488–3498.
[73] M.C. Biesinger, B.P. Payne, L.W. Lau, A. Gerson, R.S.C. Smart, X-ray photoelectron spectroscopic chemical state quantification of mixed nickel metal, oxide and hydroxide systems, Surf. Interface Anal. 41 (4) (2009) 324–332.
[74] S. Lee, S. Ha, Revealing enhanced active oxygen formation by incorporating chromium into nickel hydroxide nanosheets for improved oxygen evolution reaction, J. Phys. Chem. Lett. 15 (40) (2024) 10230–10236.
[75] Y. Jin, S. Huang, X. Yue, C. Shu, P.K. Shen, Highly stable and efficient non-precious metal electrocatalysts of Mo-doped NiOOH nanosheets for oxygen evolution reaction, Int. J. Hydrogen Energy 43 (27) (2018) 12140–12145.
[76] K. Reuter, M. Scheffler, Composition, structure, and stability of RuO_2 (110) as a function of oxygen pressure, Phys. Rev. B 65 (3) (2001) 035406.
[77] K. Reuter, M. Scheffler, Composition and structure of the RuO_2 (110) surface in an O_2 and CO environment: implications for the catalytic formation of CO_2, Phys. Rev. B 68 (4) (2003) 045407.
[78] C. Di Valentin, G. Pacchioni, A. Selloni, Theory of carbon doping of titanium dioxide, Chem. Mater. 17 (26) (2005) 6656–6665.
[79] O. Diaz-Morales, I. Ledezma-Yanez, M.T. Koper, F. Calle-Vallejo, Guidelines for the rational design of Ni-based double hydroxide electrocatalysts for the oxygen evolution reaction, ACS Catal. 5 (9) (2015) 5380–5387.